



Ultrathin nanosheets of molecular sieve SAPO-5: A new photocatalyst for efficient photocatalytic reduction of CO₂ with H₂O to methane

Shuying Zhu^a, Shijing Liang^{a,b}, Ying Wang^a, Xiaoyan Zhang^a, Fuying Li^a, Huaxiang Lin^a, Zizhong Zhang^{a,*}, Xuxu Wang^{a,*}

^a State Key Laboratory of Photocatalysis on Energy and Environment, Fuzhou University, Fuzhou 350002, PR China

^b Department of Environmental Science and Engineering, Fuzhou University, Minhou, Fujian 350108, PR China

ARTICLE INFO

Article history:

Received 28 September 2015

Received in revised form

28 December 2015

Accepted 4 January 2016

Available online 6 January 2016

Keyword:

SAPO-5

Molecular sieve

Nanosheet

CO₂ reduction

Photocatalysis

ABSTRACT

Two-dimensional (2D) SAPO-5 nanosheets with a thickness of about 3.0 nm were fabricated successfully by a facile one-pot hydrothermal method for the first time. The structure and the physicochemical properties of the as-prepared SAPO-5 nanosheets were characterized in detail. The SAPO-5 ultrathin nanosheets have great potential applications for the highly efficient reduction of CO₂ into a renewable hydrocarbon fuel. Compared with SAPO-5 microrods, the ultrathin SAPO-5 nanosheets show higher photocatalytic activity (about 6 times) for reducing CO₂ into CH₄. It is found that a large number of surface active sites on the nanosheets make it suitable for the catalytic reaction, and the ultrathin geometry of the nanosheets promotes the mass transfer of reactants and products. The normalized time-resolved fluorescence decay signals of the photo-induced absorption recorded from the SAPO-5 nanosheets and rod indicate that the excited state can survive longer on the nanosheets, which also contributes to its high photocatalytic activity. Meanwhile, high CO₂ adsorption capacity may be one important reason for high photocatalytic activity of SAPO-5 nanosheets. The reaction intermediates are detected by *in-situ* FT-IR spectroscopy. Finally, a probable mechanism is proposed based on the experimental results. It is hoped that our work could facilitate the fabrication of molecular sieve materials for solar energy conversion of CO₂.

© 2016 Elsevier B.V. All rights reserved.

1. Introduction

Nowadays, the development of clean energy sources and CO₂ recycling are crucial approaches to the depletion of fossil resources and climate change induced by an increase in CO₂ emissions, solar energy is an ideal and realistic way to achieve these goals [1–3]. To date, most of the current approaches to achieve this transformation are based on the traditional semiconductor photocatalysts, such as TiO₂, CdS and ZnGa₂O₄ etc [4–6]. Little attention was paid to the non-traditional semiconductor materials, such as zeolite molecular sieves, layered double hydroxides (LDHs) etc.

Zeolite molecular sieve characterized by their inherent large surface areas, ordered nanoscale voids and modifiable active sites are very important porous crystalline materials [7–9]. For CO₂ reduction, a variety of zeolites have been investigated as photocatalyst over the past decades [10,11]. Anpo et al. reported that transparent Ti-containing mesoporous silica thin film shows good

photocatalytic activity for the reduction of CO₂ with H₂O [12]. They explained by the charge transfer excited state [Mⁿ⁻¹-O]^{*} [8]. Mesoporous silicate ZrCu(I)-MCM-41 is capable of photochemical splitting CO₂ to CO by Frei et al. [13]. However, the photocatalytic activity of the non-traditional semiconductor materials is often very poor due to their relatively less number of active sites. Undoubtedly, new strategies must be explored to further promote the photocatalytic activity.

SAPO-5 is a silicoaluminophosphate molecular sieve with AFI structure formed from partial replacement of phosphorus atoms of the aluminium phosphate (AlPO-5) by silicon atoms [14–17]. The silicon substitution leads AlPO-5 to a charge unbalanced framework, which is advantageous to the activation of substrate molecules (CO₂ and H₂O) [18]. Moreover, the [Al³⁺-O²⁻] unites present in zeolite framework could play a similar role as that of photogenerated electron-hole pairs on the semiconductor [19,20]. Accordingly, SAPO-5 as a catalyst is feasible for photoreduction CO₂. However, conventional molecular sieves have a large crystal size in micron level [21], which leads to (1) weak CO₂ adsorption in the presence of H₂O vapor when the reaction was operated in the solid-gas interface; (2) limiting the mass transfer of the reactants

* Corresponding authors.

E-mail addresses: z.zhang@fzu.edu.cn (Z. Zhang), xwang@fzu.edu.cn (X. Wang).

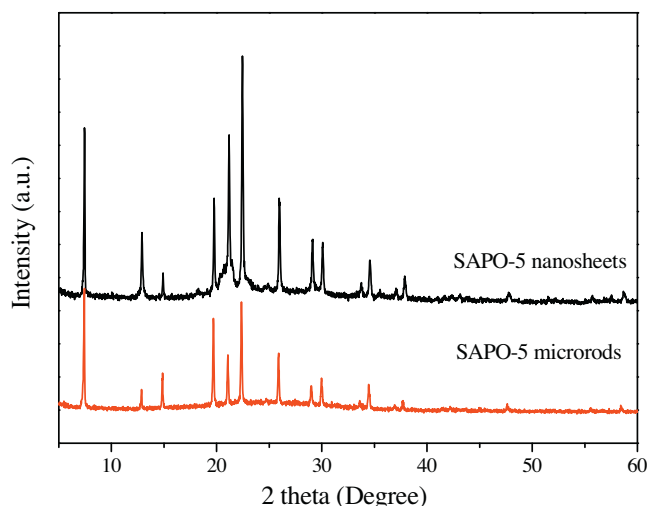


Fig. 1. XRD patterns of SAPO-5 microrods and SAPO-5 nanosheets.

and products, and (3) reducing the surface excited state. This affects adversely their catalytic activity. Two-dimensional (2D) assembling may be an alternative way to overcome these disadvantages [6,22–26]. This can increase the exposure of active site and thus improve the mass transfer process of CO_2 , finally improve the reaction efficiency. So, it is highly desirable to develop a facile strategy to fabricate an ultrathin molecular sieve nanosheet.

Herein, we first time report a facile synthesis of SAPO-5 ultrathin nanosheet by one-pot hydrothermal method, and use it as the photocatalyst for the reduction of CO_2 in the present of H_2O . The structure and morphology of the sample are characterized by XRD, TEM and AFM. Compared with SAPO-5 microrods, SAPO-5 nanosheets show higher activities. This result is attributed to high CO_2 adsorption capacity, more reactive sites and longer excited state lifetime on SAPO-5 nanosheets. In addition, the nanosheets are benefit for the mass transfer process of CO_2 . This catalyst design concept provides a new strategy for developing highly efficient photocatalysts, which will have potential for their wide range of applications in industry.

2. Experimental

2.1. Synthesis of SAPO nanosheets

Pseudoboehmite, orthophosphoric acid and tetraethyl orthosilicate (TEOS) were used as the source of aluminium, phosphorus and silicon, respectively. The optimized molar ratio of raw materials is triethylamine: Al_2O_3 : P_2O_5 : SiO_2 : H_2O = 1.2: 1: 1: 0.4: 60 for SAPO. The optimum amount of pseudoboehmite was dissolved in a mixture of orthophosphoric acid and water. Prior to adding the silicon source (TEOS), the solution was stirred for 30 min until the slurry becomes homogenous. Finally, the templates triethylamine (TEA) were added to the homogenous gels followed by stirring for 3 day. The mixture was transferred into a Teflon-lined stainless steel autoclave, sealed and heated to 200°C for 24 h. The as-synthesized product was washed with water several times followed by drying at 60°C overnight. Finally, the resulted samples were calcined in air at 600°C for 6 h in order to remove the surfactant.

2.2. Synthesis of SAPO-5 microrods

SAPO-5 rods were synthesized as per the aforementioned procedure where a molar gel composition is triethylamine: Al_2O_3 : P_2O_5 : SiO_2 : H_2O = 1: 1: 1: 0.2: 40. In a typical synthesis operation,

a known quantity of aluminium isopropoxide (2.325 g) was dissolved in distilled water (3.1 mL) and was allowed to age overnight. The gel was stirred for an hour followed by adding dropwise a dilute orthophosphoric acid (1.31 g of 85 wt% ortho-phosphoric acid in 2.5 mL distilled water) to the gel. The solution was stirred for 1 h until it became transparent. The required quantity (0.575 g) of structure directing agent, TEA, was added to this mixture, followed by stirring for 1 h. Finally, TEOS (0.238 g) was added to the mixture and then stirring was continued for another 1 h. The resultant final gel was subjected to crystallization at 180°C for 24 h in a Teflon-lined stainless steel autoclave. The as-synthesized product was washed with water several times followed by drying at 60°C overnight. Finally, the resulted samples were calcined in air at 600°C for 6 h in order to remove the surfactant.

2.3. Characterization

Transmission electron microscopy (TEM) images were recorded using a JEOL model JEM 2010 EX microscope at an accelerating voltage of 200 kV. The X-ray diffraction (XRD) measurements were performed on a Bruker D8 Advance X-ray diffractometer using $\text{Cu K}\alpha 1$ radiation ($\lambda = 1.5406 \text{ \AA}$). The amounts of Al in the products were measured by an inductively coupled plasma optical emission spectrometer (ICP-OES) (Ultima2, Jobin Yvon Co., France). The Brunauer-Emmett-Teller (BET) surface area and the CO_2 adsorption were measured with an ASAP2020M apparatus (Micromeritics Instrument Corp., USA). The nitrogen adsorption and desorption isotherms were measured at -196°C , and CO_2 adsorption isotherms were measured at 0°C . Diffuse reflection spectra (DRS) of the samples were recorded on a Varian Cary-500 spectrophotometer. In situ CO_2 -adsorbed FT-IR experiments were carried out on a Nicolet 670 FT-IR spectrometer at a resolution of 4 cm^{-1} and 32 scans. The light/dark short circuit photocurrent response was recorded with a BAS Epsilon workstation. X-ray photoelectron spectroscopy (XPS) measurements were conducted on a PHI Quantum 2000 XPS system equipped with an Al X-ray source (1486.6 eV). The time-resolved photoluminescence decay was investigated on an Edinburgh FLS 980 photoluminescence spectrometer (Edinburgh, UK). A tapping-mode atomic force microscopy (AFM, Nanoscope Multimode IIIa, Veeco Instruments) with Si-tip cantilever was used to evaluate the morphology of the obtained nanosheets on the mica substrate.

2.4. Photocatalytic activity measurement

The photocatalytic reduction of CO_2 was performed in a 40 mL Schlenk quartz glass flask reactor at ambient temperature under atmospheric pressure. The top of the reactor was sealed with a silicone rubber septum. Sampling was made intermittently through the septum during experiments. In a typical photocatalytic experiment, 10 mg solid photocatalyst was loaded in the reactor. This system was subjected to vacuum degassing and then backfilling with pure CO_2 gas. This process was repeated three times, and after the last cycle the flask was backfilled with CO_2 (1 bar). 6 μL of liquid water was introduced into the flask with a syringe via the septum. Then liquid water was gasified by heating with a hair dryer. The photocatalytic reaction was typically carried out for 4 h under two 4 W 254 nm (Philips Co., TUV 4W/G4 T5) light irradiation. The temperature of the reaction system was kept at 298 K. 0.5 mL of gas was taken from the reactor for subsequent gas concentration analysis using a gas chromatography (GC-7890A, Shimadzu) equipped with a flame ionized detector (FID). Product gases were calibrated with a standard gas mixture and their identity determined using the retention time.

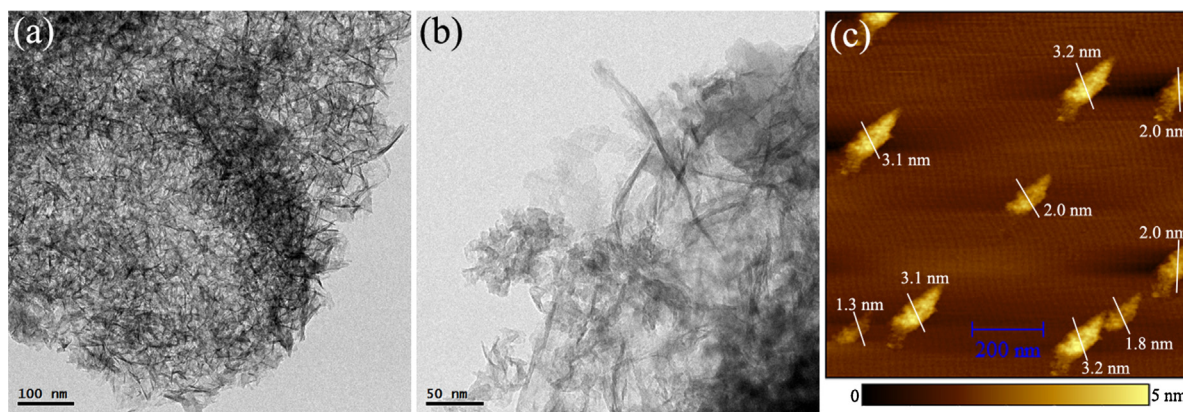


Fig. 2. TEM image (a, b) and AFM image (c) of the SAPO-5 nanosheets.

3. Results and discussion

3.1. Catalyst characterization

The XRD pattern of the as-prepared SAPO-5 nanosheets and SAPO-5 microrods are shown in Fig. 1. The XRD profiles of the two SAPO-5 samples can be well indexed to the pure SAPO-5 with AFI-type [14,27]. Obviously, the SAPO-5 nanosheet exhibits better crystallinity than the SAPO-5 microrod. No diffraction peaks from impurities and/or other phases can be detected.

The transmission electron microscopy (TEM) images of the as-synthesized SAPO-5 ultrathin nanosheets were shown in Fig. 2a and b. It can be clearly seen that the SAPO-5 sample shows morphology of ultrathin nanosheets, which is similar to graphene with a large area of wrinkled and nearly transparent nanosheets. These ultrathin nanosheets are irregular, which made of the aggregates of numerous randomly arranged nanosheets. In order to observe the nanosheets clearly, the thickness of nanosheets was evaluated by a tapping-mode atomic force microscopy (AFM) to be as thin as 3 nm (Fig. 2c). These results suggest a good quality of the as-synthesized molecular sieve ultrathin nanosheets. The SAPO-5 sample can be observed as morphology of microrods, as shown in Fig. 1S. Many irregular microrods assemble together to the formation of larger particles. In comparison to microrods, the 2D scaffolding configuration can offer an extremely high percentage of active sites for the photocatalytic reaction [26], which are beneficial for photocatalytic performance.

Fig. 3 shows the N_2 adsorption-desorption isotherms and the corresponding pore-size distribution curves of SAPO-5 nanosheets and SAPO-5 microrods. It is seen from Table 1 that the BET surface area of SAPO-5 nanosheets is slightly lower than that of the SAPO-5 microrods. And both the SAPO-5 samples show typical type IV isotherm with a hysteresis loop according to the IUPAC classification [28,29]. The feature of isotherm is usually considered to relate with the slit-like mesopores formed by sheet-like particles [30,31]. The corresponding BJH pore size distribution curve was calculated from the adsorption branch (insert in Fig. 3). The relatively narrow pore size distribution at 45–50 nm suggests the uniform size of nanosheets.

The UV–vis absorption spectra of two samples are shown in Fig. 4. A broad absorption band occurs in the range of 200–380 nm, indicating that SAPO-5 adsorbs only UV light. The photoabsorption feature is usually ascribed to the ligand-to-metal charge transfer (LMCT) involving an electron transfer from O^{2-} to Al^{3+} in the framework Al–O unit [32]. Thus, the framework Al–O units are considered to absorb UV light to induce photoreduction reaction, which have been reported by Yuko Kato [32]. It can also be seen that the SAPO-5 nanosheets show stronger photoabsorption than the

SAPO-5 microrods, which could be attributed to large fraction of exposed Al–O unit on the 2D structure. It can be anticipated that the nanosheets have more active framework Al–O units and therefore is favorable for the photocatalytic reaction.

The surface compositions and elemental valences of the SAPO-5 microrods and the SAPO-5 nanosheets were analyzed by XPS. Fig. 5a

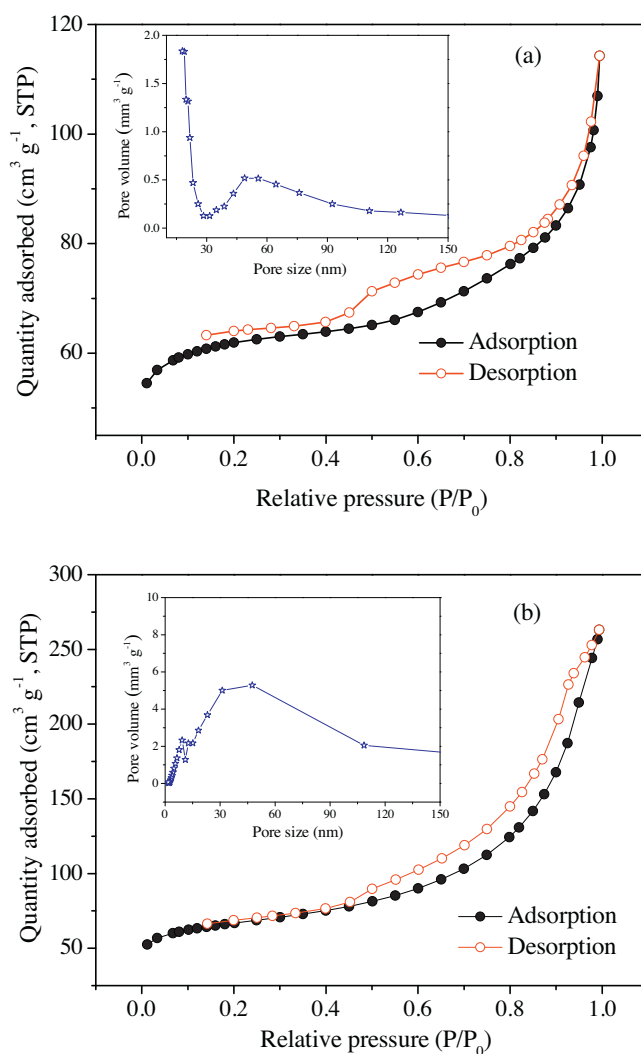


Fig. 3. Nitrogen adsorption-desorption isotherms and the corresponding pore-size distribution curves (inset) for SAPO-5 microrods (a) and SAPO-5 nanosheets (b).

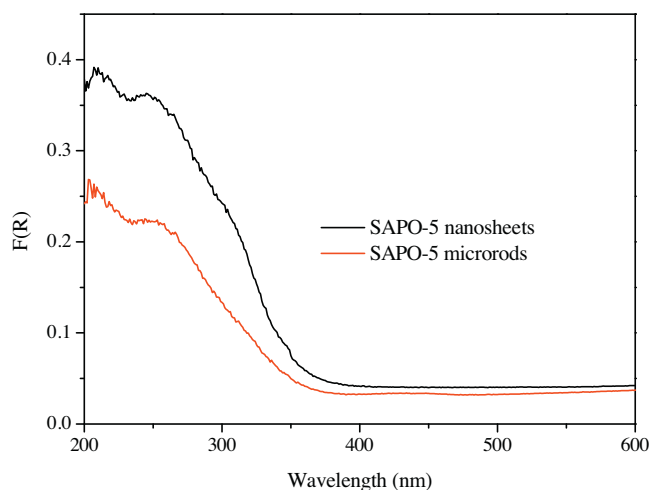
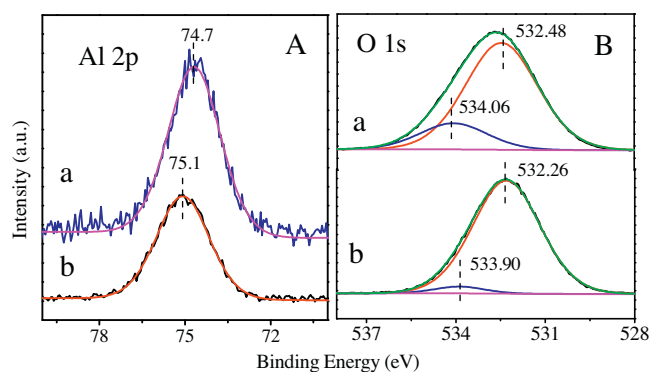
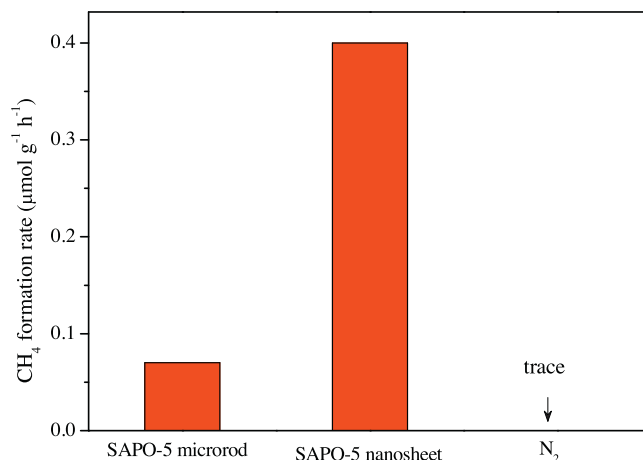
Table 1

Comparison of the physical properties and photocatalytic activity of SAPO-5 microrods and SAPO-5 nanosheets.

Sample	A_{BET}^a (m ² g ⁻¹)	$C_{\text{CO}_2}^b$ (cm ³ g ⁻¹)	$C_{\text{CO}_2}^c$ (10 ⁻² cm ³ m ⁻²)	$R_{\text{CH}_4}^d$ (μL h ⁻¹ g ⁻¹)	$R_{\text{CH}_4}^e$ (10 ⁻² μL h ⁻¹ m ⁻²)	Al(wt%)	$R_{\text{CH}_4}^f$ (10 ⁻² μL h ⁻¹ g ⁻¹)
SAPO-5 microrod	229.4	4.04	0.018	1.57	0.007	0.24	6.54
SAPO-5 nanosheet	208.8	12.9	0.062	8.96	0.043	0.27	33.19

^a BET surface area.^b Adsorbed capacity of CO₂.^c CO₂ adsorbed capacity normalized with surface area.^d Production rate of CH₄.^e Production rate of CH₄ normalized with surface area.^f Production rate of CH₄ normalized with Al content.

is the high-resolution XPS spectra of Al 2p. The nanosheets show a peak located at 74.7 eV, which is belonged to Al 2p [33,34]. But the microrods show an Al 2p peak at the binding energy of 75.1 eV. The decrease of chemical state of Al 2p from 75.1 to 74.7 eV indicates clearly that the electron density of Al atoms on nanosheet surface is higher than that of SAPO-5 microrods. In addition, the O1s peak of both samples could be deconvoluted into two peaks assigned to the lattice oxygen and surface oxygen (including –OH) [35,36], respectively, as shown in Fig. 5b. It can be seen that the O 1s binding energies of SAPO-5 microrods are 0.22 eV lower than those of nanosheets. This result shows clearly that the oxygen atoms of SAPO-5 nanosheets have lower electron density than that of the SAPO-5 microrods. Combination of the O 1s analysis with Al 2p result suggest more electrons transferring from O to Al for the nanosheets, which supports the results of DRS. It is concluded that

**Fig. 4.** UV-vis DRS of the SAPO-5 microrods and the SAPO-5 nanosheets.**Fig. 5.** High-resolution XPS spectra of the Al 2p (A) and O1s (B) of SAPO-5 nanosheets (a) and microrods (b).**Fig. 6.** Comparison of the average formation rates of CH₄ during 4 h between SAPO-5 microrods and SAPO-5 nanosheets.

SAPO-5 nanosheets can offer more adsorption and active sites for CO₂ photoreduction.

3.2. Photocatalytic reduction of CO₂

Photocatalytic reduction of CO₂ with H₂O was performed in a gas-solid system. Fig. 6 shows photocatalytic CH₄-production performance of the SAPO-5 microrods and SAPO-5 nanosheets by 254 nm light illumination. CH₄ is observed to be an only detectable reaction product for the reaction. Two control experiments were also made with catalyst in dark or without the photocatalyst under UV irradiation, respectively. No CH₄ was detected under these conditions. This means that both light and photocatalysts are necessary for the reduction of CO₂ to CH₄. The SAPO-5 microrods show a low activity for photoreduction CO₂, and CH₄ production rate is at 0.07 μmol h⁻¹ g⁻¹. In sharp contrast, the production rate of CH₄ over SAPO-5 nanosheets reaches at 0.4 μmol h⁻¹ g⁻¹, which is nearly 6 times higher than that of SAPO-5 microrods. This demonstrates that the ultrathin SAPO-5 nanosheets are much more active than the microrods for the photocatalytic reduction of CO₂. The structure or physico-chemical properties of the catalyst after photocatalytic reaction have been investigated. As showed by XRD and XPS (Fig. S2 and S3), no obvious change in the crystal structure and chemical state was observed for the SAPO-5 nanosheets after CO₂ reduction reaction. Thus, SAPO-5 nanosheets are highly stable for photocatalytic CO₂ conversion.

In order to gain insight into the effect of the texture on the photocatalytic activities, we normalized the photocatalytic reduction rates with the surface areas (Table 1). It can be seen that the surface area is not responsible for the difference in photocatalytic activity of samples, because the nanosheets with lower surface area show higher normalized reaction rates. Therefore, the increased activity on the nanosheets may be related to changes in other physicochemical properties, such as the enhancement of alkalinity, high mass

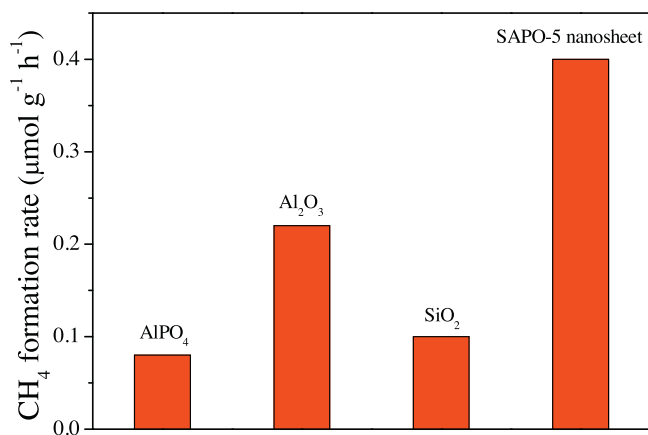


Fig. 7. CH₄ evolution rates on the AlPO₄, Al₂O₃, SiO₂, and SAPO-5 nanosheet samples.

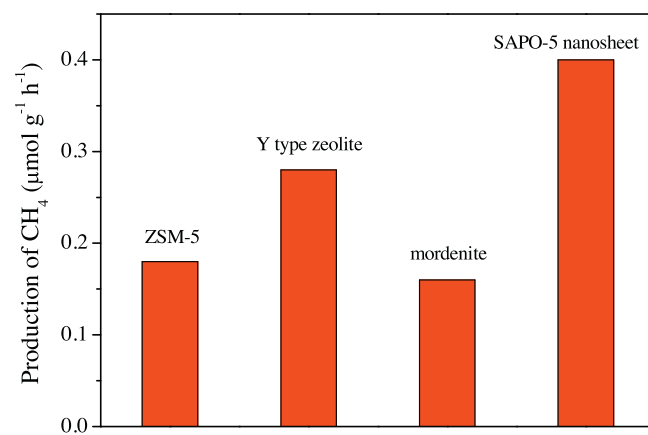


Fig. 8. CH₄ evolution rates on the ZSM-5, Y-type zeolite, mordenite and SAPO-5 nanosheet samples.

transfer efficiency of CO₂, and exposure of active sites. Moreover, no CH₄ is observed to evolve when N₂ instead of CO₂ was filled in the reaction system, which indicates that the evolved CH₄ indeed originates from photoreduction of CO₂.

The Al contents of the samples were determined by ICP, as shown in Table 1. The Al content is comparable for two samples. For comparison, we normalize the photocatalytic reduction rates with Al content (Table 1). It can be seen that the normalized rates on the nanosheets is much higher than that on the microrods. This means that the photocatalytic activity of samples is dependent on the chemical states of Al atoms. The Al atoms located at the 2D structure are more active than those at rods. Since SAPO-5 consists of elements Si, Al and P, control experiments with SiO₂, AlPO₄ and Al₂O₃ as photocatalysts are needful in the same condition. As shown in Fig. 7, except for the SAPO₅ nanosheets, other samples show poor yields of CH₄. This implies that the photocatalytic activity of SAPO-5 is due to tetrahedral coordination states of Al atoms in the AFI structure. Fig. 8 is the comparison of the photocatalytic activity among four zeolite molecular sieves including ZSM-5, Y-type zeolite, mordenite and SAPO-5 nanosheets. It can be seen that the SAPO-5 nanosheets show the highest yield of CH₄ in all samples. The difference suggests that the photocatalytic activity is decided not only by the tetrahedral coordination state of Al atoms, but also related to the properties of the ligands of Al atoms.

It has been revealed that for metal oxides, the oxygen vacancies can behave as adsorptive and catalytic sites in heterogeneous catalysis [37–39]. In order to explore surface defects of SAPO-5, EPR spectra of the SAPO-5 microrods and nanosheets were determined at 77 K, as shown in Fig. 9a. The nanosheets show a strong

EPR signal at g-values of around 2.003, which are attributed to the oxygen vacancies [40,41]. But for SAPO-5 microrod sample, no signal of oxygen vacancy is observed. This result suggests that abundant oxygen defects are present on the SAPO-5 nanosheets. The high catalytic activity of nanosheets may be attributed to the affluent surface defects, which act as active sites [40,42]. Fig. 9b shows the EPR spectra of SAPO-5 nanosheet sample in air and CO₂ atmospheres, respectively. The lower intensity of V_o signal in CO₂ atmosphere than in air can be attributed to more efficient CO₂ adsorption over the oxygen vacancies [40,43,44]. This indicates that SAPO-5 nanosheets have a higher CO₂ adsorption capacity, which promotes CO₂ mass transfer and finally improves the photocatalytic activity.

CO₂ adsorption isotherms on the SAPO-5 nanosheets and SAPO-5 microrods are measured at 273 K under 1 atm, as shown in Fig. 10. It can be seen that the nanosheets exhibit higher CO₂ adsorption capabilities than the microrods. For the SAPO-5 nanosheets, the adsorption amount of CO₂ reaches up to 12.9 g cm⁻³, while the adsorption amount is only 4.04 g cm⁻³ for the SAPO-5 microrods. To rule out the effect of surface areas on their CO₂ adsorption capabilities, we normalized the CO₂ adsorption capabilities with the surface areas (Table 1). It can be seen that the order of the normalized CO₂ adsorption capacities is unchanged. This is, the increased adsorption amount of CO₂ is not contributed by the specific surface area. For SAPO-5 nanosheets, the surface oxygen vacancies and electron-rich Al atoms may be responsible for its high CO₂ adsorption.

Photocurrent response of SAPO-5 microrods and SAPO-5 nanosheets on ITO-coated glass electrodes are determined by

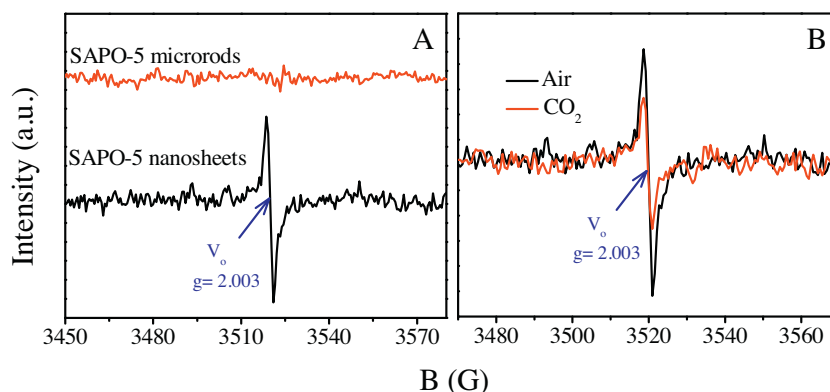


Fig. 9. EPR spectra of the SAPO-5 microrods and SAPO-5 nanosheets under dark condition (A), and in air and CO₂ atmosphere for SAPO-5 nanosheets (B).

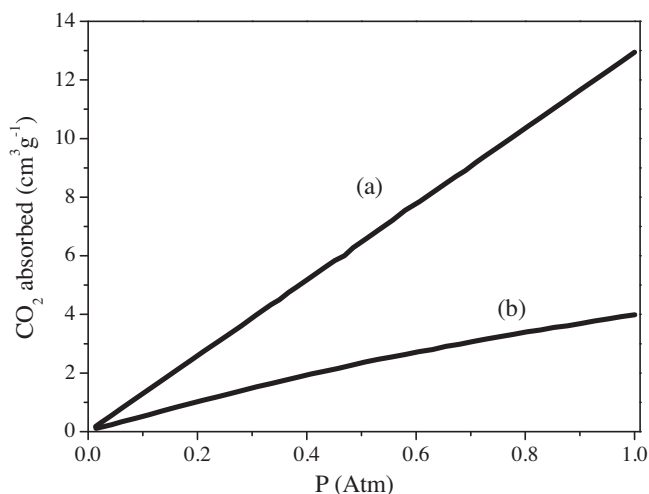


Fig. 10. CO_2 adsorption isotherms of the SAPO-5 microrods (a) and SAPO-5 nanosheets (b) at 273 K in 1 atm pressure.

254 nm light irradiation, as shown in Fig. 11. The SAPO-5 nanosheet electrode shows higher cathodic photocurrent than SAPO-5 rod electrode. This indicates that the excited state electrons over SAPO-5 nanosheet electrode can be captured more quickly, which agrees well with the high photocatalytic activity of SAPO-5 nanosheet. Thus, we can also ascribe the enhancement of photocatalytic performance over SAPO-5 nanosheets to the increased concentration of excited state electrons and a better electron transfer rate over 2D nanosheet.

To gain a further insight into the higher photoactivity of the nanosheets, the excited state transfer dynamics were investigated by the transient absorption spectroscopy. The photoluminescence decay profiles of the SAPO-5 nanosheets and microrods are shown in Fig. 12. Obviously, the SAPO-5 nanosheet shows slower decay kinetics than the SAPO-5 microrods. In other word, the life time of the excited state over nanosheets was longer than that of the SAPO-5 microrods. According to the fitting calculation of the decay spectrum, it is estimated that the excited state lifetime of the SAPO-5 nanosheets and the SAPO-5 microrods are 4.8 ns and 3.6 ns, respectively. Longer lifetime of the excited state over SAPO-5 nanosheet makes a contribution for it higher photocatalytic activity.

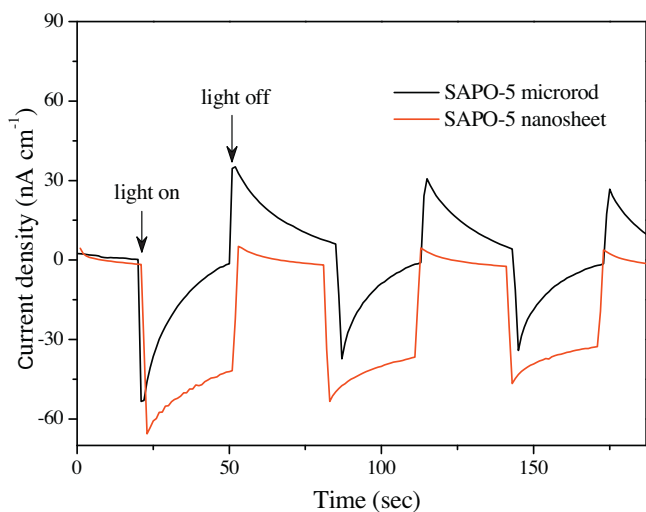


Fig. 11. Periodic on/off photocurrent response of the SAPO-5 microrod and SAPO-5 nanosheet electrodes in 0.2 M Na_2SO_4 electrolyte with zero bias versus Ag/AgCl.

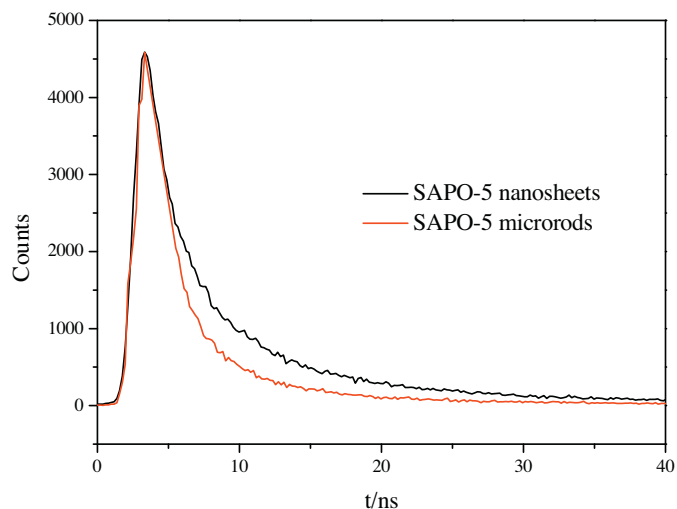


Fig. 12. Time-resolved fluorescence decay spectra of the SAPO-5 microrods and SAPO-5 nanosheets.

In order to better understand the effect of the adsorption and mass-transfer of CO_2 on the photocatalytic process, in situ FT-IR analyses have also been done. As shown in Fig. 13, both the nanosheets and microrods show a CO_2 adsorption peak at 1261 cm^{-1} , which is ascribed to CO_2^- bonded to the surface [24,45–47]. For the SAPO-5 microrods, the IR absorption band after and before UV irradiation is almost unchanged. But for the SAPO-5 nanosheets, the intensity is visibly decreased under 254 nm light irradiation. This can be indicative of fast mass-transfer of CO_2 on the sample, or the surface CO_2^- as active intermediate of CO_2 reduction on the SAPO-5 nanosheets.

For SAPO-5, the 2D configuration of nanosheets can provide an extremely high percentage of exposed Al atoms as an alkaline site for more efficient adsorption of acidic CO_2 molecules. The nanosheet structure enables the excited state electrons to be captured and transferred more quickly, as verified by the enhanced photocurrent response on SAPO-5 nanosheets. Moreover, from the EPR results, we can observed the presence of abundant oxygen

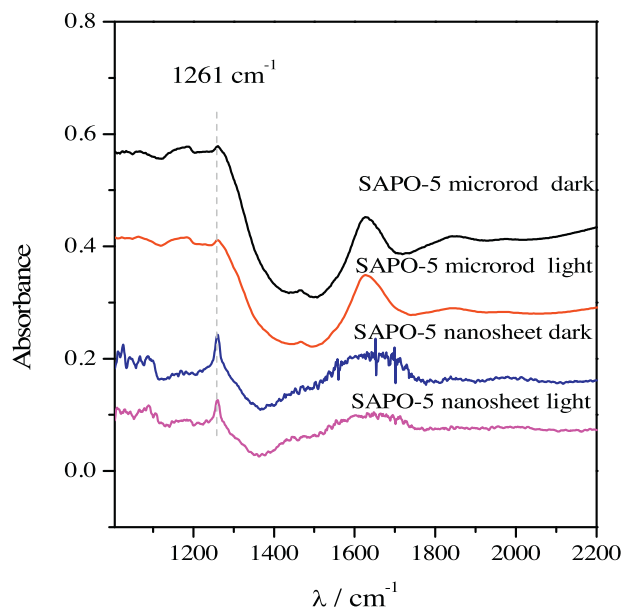


Fig. 13. In-situ FT-IR spectra of the SAPO-5 microrods and nanosheets upon adsorption of CO_2 and H_2O in dark and under irradiation with 254 nm light.

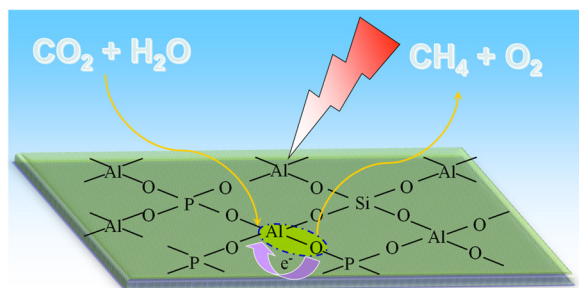
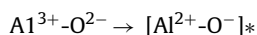


Fig. 14. Possible mechanism for the photoreduction CO₂ over the SAPO-5 nanosheets.

defects (V_o) on the SAPO-5 nanosheets. The CO₂ introduction can lower the intensity of V_o signal, indicating the interaction between CO₂ and V_o to promote CO₂ mass transfer. All these induce longer lifetime of the excited state over SAPO-5 nanosheet, and therefore higher photocatalytic activity. However, its photocatalytic mechanism is an issue, which cannot be dodged. According to the DRS spectrum, the SAPO-5 can be regarded as a UV-light-active material. For such materials, the photocatalytic mechanism has been explained by the ligand-to-metal charge-transfer excitation. The M-O species may be excited by UV or visible light to produce a charge-transfer excited state $[M^{(n-1)+}-O^-]^*$, which leads to photocatalytic reactions [48]. Based on the above experimental results and the analysis, it is suggested that the photocatalytic reduction of CO₂ over SAPO-5 nanosheets may occur through the possible mechanism illustrated in Fig. 14. Under 254 nm light irradiation, the Al-O isolated units of SAPO-5 were excited to form an excited state $[Al^{2+}-O^-]^*$, which can be written as



The Al^{2+} and O^- atoms in the $[Al^{2+}-O^-]^*$ as active sites are analogous to the electron and hole pairs on the photoinduced semiconductor, and they play roles of reduction and oxidation, respectively. Excited state electron can be quickly transfer to absorbed CO₂, forming the $\bullet CO_2^-$. Finally, the activated $\bullet CO_2^-$ would transform into CH₄ via a photogenerated electron-induced multistep reduction process. Higher activity of SAPO-5 nanosheets than SAPO-5 microrods can be explained by the following reasons. (1) XPS results suggested that electron density of the Al atoms on the nanosheet surface is higher than that of SAPO-5 microrods, which indicates basicity increase of the exposed Al atom on nanosheets. The basicity increase is more efficient for adsorption of acidic CO₂ molecules. (2) The nanosheet structure facilitates the photogenerated electrons to separate and transfer to CO₂ for reduction reaction. (3) Abundant oxygen defects present on the SAPO-5 nanosheets as an active site can enhance adsorption and mass transfer of CO₂.

4. Conclusions

In summary, the two-dimensional SAPO-5 nanosheet with 3.0 nm size was successfully fabricated for the first time by the one-pot hydrothermal method. The SAPO-5 nanosheets exhibited greatly enhanced photocatalytic activity compared with SAPO-5 microrods for CO₂ fixation under 254 nm light irradiation. The photocatalytic mechanism on SAPO-5 could be explained by $[Al^{2+}-O^-]^*$ units as photoactive sites. The remarkable enhancement in the photocatalytic activity of nanosheets is attributed to synergetic effect of two factors as follow, (1) higher adsorption amount of CO₂ molecules, and (2) more abundant surface active sites. The present work affirmed that phosphate molecular sieve ultrathin nanosheets

may be potential photocatalysts for the reduction of CO₂ to CH₄, and modifying nanosheets for enhancing activity is undergoing.

Acknowledgements

The work is financially supported by the National Natural Science Foundation of China (Grants No. 21173044, 21303019, U1305242), the Natural Science Foundation of Fujian Province (2014J05016), the Technology Project of Education Office of Fujian Province of PR China (JA12036 and JA14030) and National Basic Research Program of China (973 Program, No. 2014CB260410).

Appendix A. Supplementary data

Supplementary data associated with this article can be found, in the online version, at <http://dx.doi.org/10.1016/j.apcatb.2016.01.002>.

References

- [1] T. Ohno, T. Higo, N. Murakami, H. Saito, Q. Zhang, Y. Yang, T. Tsubota, *Appl. Catal. B: Environ.* 152–153 (2014) 309–316.
- [2] S.K. Kang, D.J. Choi, S.M. Ham, W. Ji, D.S. Han, H. Abdel-Wahab, *Energy Environ. Sci.* 8 (2015) 2638–2643.
- [3] X. Meng, T. Wang, L. Liu, S. Ouyang, P. Li, H. Hu, T. Kako, H. Iwai, A. Tanaka, J. Ye, *Angew. Chem. Int. Ed.* 53 (2014) 11478–11482.
- [4] W.-N. Wang, W.-J. An, B. Ramalingam, S. Mukherjee, D.M. Niedzwiedzki, S. Gangopadhyay, P. Biswas, *J. Am. Chem. Soc.* 134 (2012) 11276–11281.
- [5] Y. Ma, X. Wang, Y. Jia, X. Chen, H. Han, C. Li, *Chem. Rev.* 114 (2014) 9987–10043.
- [6] Q. Liu, D. Wu, Y. Zhou, H. Su, R. Wang, C. Zhang, S. Yan, M. Xiao, Z. Zou, *ACS Appl. Mater. Interfaces* 6 (2014) 2356–2361.
- [7] R.I.J. Amos, F. Heinroth, B. Chan, A.J. Ward, S. Zheng, B.S. Haynes, C.J. Easton, A.F. Masters, T. Maschmeyer, L. Radom, *ACS Catal.* (2015) 4353–4362.
- [8] Y. Shioya, K. Ikeue, M. Ogawa, M. Anpo, *Appl. Catal. A: Gen.* 254 (2003) 251–259.
- [9] M. Yang, P. Tian, C. Wang, Y. Yuan, Y. Yang, S. Xu, Y. He, Z. Liu, *Chem. Commun.* 50 (2014) 1845–1847.
- [10] H.-Y. Wu, H. Bai, J.C.S. Wu, *Ind. Eng. Chem. Res.* 53 (2014) 11221–11227.
- [11] W. Lin, H. Han, H. Frei, *J. Phys. Chem. B* 108 (2004) 18269–18273.
- [12] K. Ikeue, H. Yamashita, M. Anpo, T. Takekaki, *J. Phys. Chem. B* 105 (2001) 8350–8355.
- [13] W. Lin, H. Frei, *J. Am. Chem. Soc.* 127 (2005) 1610–1611.
- [14] A.K. Singh, R. Yadav, V. Sudarsan, K. Kishore, S. Upadhyayula, A. Sakthivel, *RSC Adv.* 4 (2014) 8727–8734.
- [15] K. Mathisen, M. Stockenhuber, D.G. Nicholson, *Phys. Chem. Chem. Phys.* 11 (2009) 5476–5488.
- [16] M. Li, C. Zeng, L. Zhang, *CrystEngComm* 14 (2012) 3787–3792.
- [17] M. Montoya-Urbina, D. Cardoso, J. Pérez-Pariente, E. Sastre, T. Blasco, V. Fornés, *J. Catal.* 173 (1998) 501–510.
- [18] Y. Iwase, K. Motokura, T.-r. Koyama, A. Miyaji, T. Baba, *Phys. Chem. Chem. Phys.* 11 (2009) 9268–9277.
- [19] G. Yan, X. Wang, X. Fu, D. Li, *Catal. Today* 93–95 (2004) 851–856.
- [20] G. Yan, J. Long, X. Wang, Z. Li, X. Wang, Y. Xu, X. Fu, *J. Phys. Chem. C* 111 (2007) 5195–5202.
- [21] X. Meng, F.-S. Xiao, *Chem. Rev.* 114 (2013) 1521–1543.
- [22] M. Guan, C. Xiao, J. Zhang, S. Fan, R. An, Q. Cheng, J. Xie, M. Zhou, B. Ye, Y. Xie, *J. Am. Chem. Soc.* 135 (2013) 10411–10417.
- [23] X. Chen, Y. Zhou, Q. Liu, Z. Li, J. Liu, Z. Zou, *ACS Appl. Mater. Interfaces* 4 (2012) 3372–3377.
- [24] Q. Zhang, C.-F. Lin, B.-Y. Chen, T. Ouyang, C.-T. Chang, *Environ. Sci. Technol.* 49 (2015) 2405–2417.
- [25] P. Niu, Y. Yang, J.C. Yu, G. Liu, H.-M. Cheng, *Chem. Commun.* 50 (2014) 10837–10840.
- [26] S. Liang, L. Wen, S. Lin, J. Bi, P. Feng, X. Fu, L. Wu, *Angew. Chem. Int. Ed.* 53 (2014) 2951–2955.
- [27] L. Wang, C. Guo, S. Yan, X. Huang, Q. Li, *Microporous Mesoporous Mater.* 64 (2003) 63–68.
- [28] Q. Lin, L. Li, S. Liang, M. Liu, J. Bi, L. Wu, *Appl. Catal. B: Environ.* 163 (2015) 135–142.
- [29] S. Zhu, S. Liang, Q. Gu, L. Xie, J. Wang, Z. Ding, P. Liu, *Appl. Catal. B: Environ.* 119–120 (2012) 146–155.
- [30] M. Kruk, M. Jaroniec, *Chem. Mater.* 13 (2001) 3169–3183.
- [31] W. Yang, J. Li, Y. Wang, F. Zhu, W. Shi, F. Wan, D. Xu, *Chem. Commun.* 47 (2011) 1809–1811.
- [32] Y. Kato, H. Yoshida, A. Satsuma, T. Hattori, *Microporous Mesoporous Mater.* 51 (2002) 223–231.
- [33] A. Arranz, C. Palacio, *Langmuir* 18 (2002) 1695–1701.
- [34] Z. Zhang, Q. Fu, H. Zhang, Y. Li, Yao, Tan, Bao, *J. Phys. Chem. C* 111 (2007) 13524–13530.

- [35] K. Tanaka, C.-K. Choo, Y. Komatsu, K. Hamaguchi, M. Yamaki, T. Itoh, T. Nishigaya, R. Nakata, K. Morimoto, *J. Phys. Chem. B* 108 (2004) 2501–2508.
- [36] M. Franco, N. Rosenbach, G.B. Ferreira, A.C.O. Guerra, W.B. Kover, C.C. Turci, C.J.A. Mota, *J. Am. Chem. Soc.* 130 (2008) 1592–1600.
- [37] W. Pipornpong, R. Wanbayor, V. Ruangpornvisuti, *Appl. Surf. Sci.* 257 (2011) 10322–10328.
- [38] J. Polarz, V. Ischenko, M.W.E. van den Berg, O. Hinrichsen, M. Muhler, M. Driess, *Angew. Chem. Int. Ed.* 45 (2006) 2965–2969.
- [39] N.M. Dimitrijevic, B.K. Vijayan, O.G. Poluektov, T. Rajh, K.A. Gray, H. He, P. Zapol, *J. Am. Chem. Soc.* 133 (2011) 3964–3971.
- [40] S. Zhu, S. Liang, Y. Tong, X. An, J. Long, X. Fu, X. Wang, *Phys. Chem. Chem. Phys.* 17 (2015) 9761–9770.
- [41] D. Zhao, A. Rodriguez, N.M. Dimitrijevic, T. Rajh, R.T. Koodali, *J. Phys. Chem. C* 114 (2010) 15728–15734.
- [42] N.A. Deskins, R. Rousseau, M. Dupuis, *J. Phys. Chem. C* 114 (2010) 5891–5897.
- [43] X. Pan, M.-Q. Yang, X. Fu, N. Zhang, Y.-J. Xu, *Nanoscale* 5 (2013) 3601–3614.
- [44] L. Liu, C. Zhao, Y. Li, *J. Phys. Chem. C* 116 (2012) 7904–7912.
- [45] H. Zhao, L. Liu, J.M. Andino, Y. Li, *J. Mater. Chem. A* 1 (2013) 8209–8216.
- [46] R.W. Stevens, R.V. Siriwardane, J. Logan, *Energ Fuel* 22 (2008) 3070–3079.
- [47] S.N. Habisreutinger, L. Schmidt-Mende, J.K. Stolarczyk, *Angew. Chem. Int. Ed.* 52 (2013) 7372–7408.
- [48] M. Anpo, M. Takeuchi, *J. Catal.* 216 (2003) 505–516.